

We are IntechOpen, the world's leading publisher of Open Access books Built by scientists, for scientists

4,800

Open access books available

122,000

International authors and editors

135M

Downloads

Our authors are among the

154

Countries delivered to

TOP 1%

most cited scientists

12.2%

Contributors from top 500 universities



WEB OF SCIENCE™

Selection of our books indexed in the Book Citation Index
in Web of Science™ Core Collection (BKCI)

Interested in publishing with us?
Contact book.department@intechopen.com

Numbers displayed above are based on latest data collected.
For more information visit www.intechopen.com



Passive Microwave Remote Sensing of Rain from Satellite Sensors

Sante Laviola and Vincenzo Levizzani

*Institute of Atmospheric Sciences and Climate – National Research Council
Bologna, Italy*

Abstract

The purpose of this chapter is to offer an accurate treatment of relevant aspects of satellite remote sensing of precipitation using passive microwave (PMW) radiometers. Microwave observations of the Earth's system differ substantially from those based on optical and infrared wavelengths. Visible (VIS) and infrared (IR) instruments essentially sense the cloud top properties by measuring reflected or emitted radiation. Microwave frequencies, on the contrary, possess greater penetrating capabilities than optical radiation and can thus be exploited to investigate cloud internal properties by retrieving the interaction of hydrometeors with the radiation field. This fact is particularly true in the remote sensing of precipitation, where the impact of the volume of raindrops on the radiative field is directly linked to the total extinction of incident radiation.

The following paragraphs will be focused on one hand on theoretical considerations at the foundations of thermal radiation processes and on the other the attention will be centered on a treatment of practical aspects of retrieving precipitation in the microwave bands.

Particular attention will be dedicated in the first part of the chapter to the radiative transfer theory in the microwaves by using the Rayleigh-Jeans formulation and a description of the absorption and scattering processes associated with the Mie theory with the approximation of extinction from poly-disperse media as proxies for natural media. This section will create a valid substrate to understand and theoretically evaluate the impact of atmospheric constituents such as precipitation types or hydrometeor phases and sizes on the natural radiation emitted from the Earth. Furthermore, the theoretical considerations of this section will be compared in the second part of the chapter with real measurements. Making use of a wide suite of microwave frequencies of a new generation of PMW sensors flying on board polar orbiting satellites the attenuation of the microwave signal due to rain clouds will be discussed possibly discerning the contribution to the total radiation of the emissivity from various surfaces falling into the satellite field of view. Finally, a new microwave high-frequency method to retrieve and classify precipitation types will be presented.

1. Introduction

Remote sensing from satellite-based sensors has established itself as the key method for the observation and monitoring of the planet Earth because of several reasons. From a practical

point of view, observations from orbital platforms guarantee continuous measurements of very wide regions of the globe especially over inaccessible areas such as impervious mountains or open oceans where measurement campaigns are often difficult, expensive and even dangerous. Scientifically speaking, since a satellite platform generally "carries" a large instrumental suite covering several frequency-channels, very diverse observations and studies can be planned at same time exploiting data from a single space mission. Finally, especially for last generation of geostationary and low-orbiting satellites, orbital sounding can be done at high temporal and spatial resolutions both day and night allowing for a continuous monitoring of a phenomenon during all its evolutionary stages. Satellite rainfall retrieval acquires even more value when associated to more conventional observing systems, which were inadequate to correctly quantify precipitating phenomena both at the local and global scales. A variety of schemes using VIS and IR satellite data have been applied to the problem of precipitation estimation (Levizzani, 2003; Levizzani et al., 2007; Hsu et al., 2007) and to retrieve cloud microphysical properties (Rosenfeld, 2007; Cattani et al., 2007). Nevertheless, due to the very low penetrating capabilities of dense medium approaches based on these are restricted to observations of cloud top. For this reason, their implementation into retrieval techniques of precipitation often result in erroneous estimations of rain amount especially during light rain episodes when cloud top temperatures are comparable to those of non-rainy clouds. Microwave radiation is, in general, affected in a minor way by most clouds, particularly for wavelengths above the centimeters. From the precipitation retrieval perspective, microwaves offer the enormous advantage to guarantee a direct relationship between the radiation field and the bulk of hydrometeors "illuminated" by the upwelling radiation. On this basis, many retrieval techniques originally thought for VIS and IR wavelengths were implemented with microwave frequencies when they became available at the end of the 1970s. Skillful combinations of observations from high spatial and temporal resolution VIS-IR geostationary sensors with rainfall-measuring capabilities of microwave radiometers are employed in the so called "blended techniques". Such methods, based on the calibration of IR brightness temperatures with microwave rain signatures (e.g., Turk & Mehta, 2007) or on the advection of microwave precipitation by using thermal IR signal (Joyce et al., 2004), are normally used to reconstruct precipitation tracks over regions not regularly covered by polar orbiting satellites. Therefore, it is quite intuitive to adopt improvement strategies microwave precipitation retrievals for their input to statistical methods as well as to numerical models. The last fifteen years have witnessed to the great progress in microwave retrieval methods as a direct consequence of the improvement of microwave orbital instruments as regards their ground resolution, which went from some hundred to few tens of kilometers, and also from the point of view of the number of available channels aboard the spacecraft. Of equal importance is the ever increasing number of flying satellites that have considerably reduced the global satellite passing time lags down to 3 hours.

In the following we present the topical aspects of microwave remote sensing of precipitation by firstly discussing the theoretical concepts and secondly applying them to some case studies. Since the aim of this work is mainly devoted to the practical application of microwave remote sensing, the argued theory will be followed by examples that describe roughly but clearly can be observed and measured from satellite in a certain situations where either absorption or scattering extinguish the incoming radiation in a medium. The second part of the chapter contains a brief description of a new technique to retrieve rainfall

based on microwave high frequencies of the five-channel passive sensor Advanced Microwave Sounding Unit-B (AMSU-B). Particularly, this method exploits rain signature within the water vapor absorption band at 183.31 GHz to infer precipitation rates and a series of thresholds to classify rain types and categorize non-rainy pixels into snow cover, cloud liquid water and small cloud droplets/water vapor classes. Finally, the performances of the method will be presented in three case studies where the model was tested in very different situations as to the genesis of the cloud system and consequently as to rainfall type and regime.

2. Fundamental principles of microwave remote sensing from satellite sensors

Passive microwave remote sensing, which has largely developed over the last few years thanks to the improvement in the spatial resolution and in the variety of channel-frequencies on board of last generation sensors, can be summarized using a few keywords: quasi-transparency, surface emissivity, absorption-scattering. This oversimplification of the problem is not due to the fact that microwave sounding is simpler than that based on other approaches such as that based on IR or VIS wavelengths, but it refers to some aspects of the observed scene that are more unambiguously identified with microwave frequencies than with other shortwave methods. This is due to the existing direct link between the measured observable and the perturbation induced to the radiation field along the wave propagation path. This signal displacement at the nominal frequency value is directly correlated to the bulk of the observed parameter. This fact will be more elucidated in section 2.2 where an overview of the radiative transfer equations in the approximation of microwaves (MRTE) will be discussed. The final part of the section will be centered on radiation extinction by absorption and scattering both from the theoretical and the observational point of view.

Nevertheless, the radiative transfer theory will be introduced by some fundamental concepts on the emissivity in section 2.1. Microwave observation is greatly susceptible to surface features: the variation of moisture content or vegetation coverage and the differences in salinity levels or the presence of sea ice drastically contaminate microwave remote sensing. Section 2.1 will propose an overview on emission properties of surfaces and an interesting example will be illustrated where a snow covered terrain shows the same scattering signal of convective clouds, thus falsely identifying an area over land as intensely precipitating.

2.1 An overview on the emissive properties of surfaces

Microwave measurements from space are extremely sensitive to a wide range of surface and atmospheric properties. Surface type, different terrain coverage and local variation of atmospheric parameters, can deeply affect space observations often introducing errors in the retrieval methods because of the incorrect evaluation of local conditions. The main goal of this section is to highlight the major “problems” that affect satellite observations with PMW sensors and in particular some examples will be shown of ambiguous situations where the same signal could be equally associated to more than one different contributor.

Unlike the thermal IR spectral region where the black body approximation often well describes the real behavior of emitters, in the microwaves an emitting surface must be considered as a grey body so that its emissivity value is usually lower than unit. An accurate

theoretical treatment of the physics of dielectric materials will be omitted since the aim of this paper is to offer a practical observational guide from satellite-based microwave sensors. We will limit ourselves to describe the effect of superficial emissivity variations by considering the observed surfaces as “cold” and “warm”. These two categorizations are by no means enough, because several intrinsic and superficial features contribute to determine the emissivity value ϵ and consequently to deviate the behavior of a real body from the Planck’s law.

The observed variability in microwave radiances for homogeneous land surfaces is normally caused by variations in skin temperature and surface emissivity, while the variability for open seawater is attributed to the atmospheric constituents such as columnar water vapor, temperature profiles and presence of cloud liquid water. These just very general considerations really contain the justification about the use of terms “cold” and “warm”. The land surface emissivity being higher ($\epsilon \approx 0.80-1.00$) than ocean’s ($\epsilon \approx 0.40-0.60$) appears as a “warm” object. Nevertheless, unlike for the ocean, land emission variability is strictly linked to the strong temporal and spatial variations of soil features as roughness, vegetation cover and moisture content. It is thus very complex to model surface properties in the microwave from arid surfaces to dense vegetation or snow and consequently it is difficult to discern between the surface and atmospheric contributors to the upwelling radiation. The impact of the different surface type on the temperature and humidity retrievals has been quantified by English (1999); in these studies microwave emission errors for different continental surfaces is evaluated by using a mathematical technique to potentially extend the low-altitude sounding information over solid surfaces. Other authors have developed computational scheme to improve the mathematical description of surface emissivity for several land types: bare soil (Shi et al., 2002), vegetation canopy (Ferrazoli et al., 2000) and snow-covered terrain (Fung, 1994).

Over open ocean the substantially stable and uniform “cold” background emphasizes more the extinction of upwelling radiation by atmospheric constituents and the contribution of various elements to the total radiation depression are reasonably well separated. Sea surface emissivity is largely determined by dielectric properties of seawater through the Fresnel equation and, especially for a drier atmosphere, the surface has a larger effect on the measured radiance. Many authors have developed models to predict the dielectric constant of seawater in order to improve the retrieval method of atmospheric parameters. Klein and Swift (1977), for example, proposed an improved model for the dielectric constant developed on the basis of measurements at L-band and S-band. Their equations provide an adequate description of the dielectric constant with an accuracy within 0.3 K but model performances largely decrease at higher microwave frequencies. Other studies based on radiometric airborne observations of the ocean-roughened surface (Guillou et al., 1996) have extended and validated existing sea emissivity models at higher frequencies 89 and 157 GHz. Likewise, laboratory experiments with an aqueous NaCl solution and synthetic seawater modeling (Ellison et al., 1998) have demonstrated that the assessment of sea surface emissivity for the interpretation of radar and radiometer data necessarily requires accurate permittivity measurements (better than 5%) of natural seawater in the frequency range 40-100 GHz.

In the last fifteen years with the increasing number of satellite platforms hosting increasingly higher spatial resolution new generation microwave sensors, the use of orbital instrument data became more widespread. A multisensor satellite approach, based on the

Defense Meteorological Satellite Program (DMSP) instrumental suite, is followed by Greenwald & Jones (1999) to compare satellite observations of ocean surface emissivity at 150 GHz together with selected permittivity models to evaluate the accuracy of retrieval schemes and the impact of atmospheric parameters on final retrievals. Stephen & Long (2005) and Banghua et al. (2008) have modeled microwave emissions of the Sahara desert by using data from the Tropical Rainfall Measuring Mission (TRMM) Microwave Imager (TMI) and the emissivity values over snowy soil with data of the Advanced Microwave Sounding Unit (AMSU) on board the National Oceanic and Atmospheric Administration (NOAA) satellites, respectively.

An example of the radiometric response of the NOAA/AMSU-B frequency range 89-190 GHz to the emission for several surface and atmospheric contributors is reported in Fig. 1. An analysis of the images in the window frequencies at 89 GHz (top-left) and 150 GHz (top-middle) evidences the striking contrast between land and open water numerically denounced by a brightness temperature discrepancy over 50 K at 89 GHz. Similarly, the coldest background widely enhances the presence of cloud liquid water at 89 GHz close to Spanish, Italian and Northern Europe coastlines. This characteristic is attenuated at 150 GHz, whose weighting function "peaks" around 1 km above surface, and thus warmer atmospheric layers partially mask cloud liquid signatures. An interesting aspect of Fig. 1 is related to the land emissivity changes. Observing the image at 150 GHz a brightening structure is extensively distributed in the middle of the image. In the same location but at 89 GHz this region is related to the Alps and Apennines whereas at 190 GHz (top-right) it almost disappears except over higher mountain tops. The similarity between satellite images and daily snow cover map unmistakably suggests that snowy terrain is the main responsible of significant reduction of the Earth's emissivity. Because of the underlying freezing surface, low-layers water vapor, which generally absorbs radiation at 150 GHz smoothing the effects of surface emissivity, is more or less totally condensed over snow cover pack forming a sort of "dry-zone" in the first layers above ground. This assertion is also corroborated by mixing ratio measurements retrieved by three sample radiosonde stations (red dots in Fig. 1). As a consequence of these drier conditions the weighting function lowers close to the surface largely enhancing the effects of scattering by ice particles of fallen snow. The final result is that the brightness temperature of the upwelling radiation reaching the satellite drastically decreases from 40 K to 70 K over the Alps and Apennines. In addition, it must be said that the signal extinction of snow cover at 150 GHz is quite similar to that of scattering by ice on cloud top with an enormous errors during rain pixel classification. A different behavior is shown in the 89 GHz channel, where the upward radiance varies from 20 K to 70-80 K over mountain with increasing surface roughness. Finally, the 190 GHz channel sounding the absorption of water vapor around 2 km in general is less affected by surface emissivity variations. Nevertheless, when local dry condition establish this frequency senses closer to the surface and it can sense more surface effects. This condition is frequently observed over polar regions where dry profiles constrain opaque frequencies around 183.31 GHz to sound atmospheric layers near the frozen surface.

Our experiments, take us to develop a series of thresholds based on a combination of the above frequencies with the scope to improve snow cover pixel detection and reduce false rain signals into the retrieval method presented in section 4.3. An example of our snow cover product, obtained by using frequencies thresholds proposed in the central part of Fig. 1, is shown on the same figure (bottom-right). The application of a snow cover filter, which

also distinguishes between wet and dry snow, has significantly reduced the number of misclassifications and gave us the possibility to apply the method also at higher latitudes with a substantial improvement of the algorithmic performances.

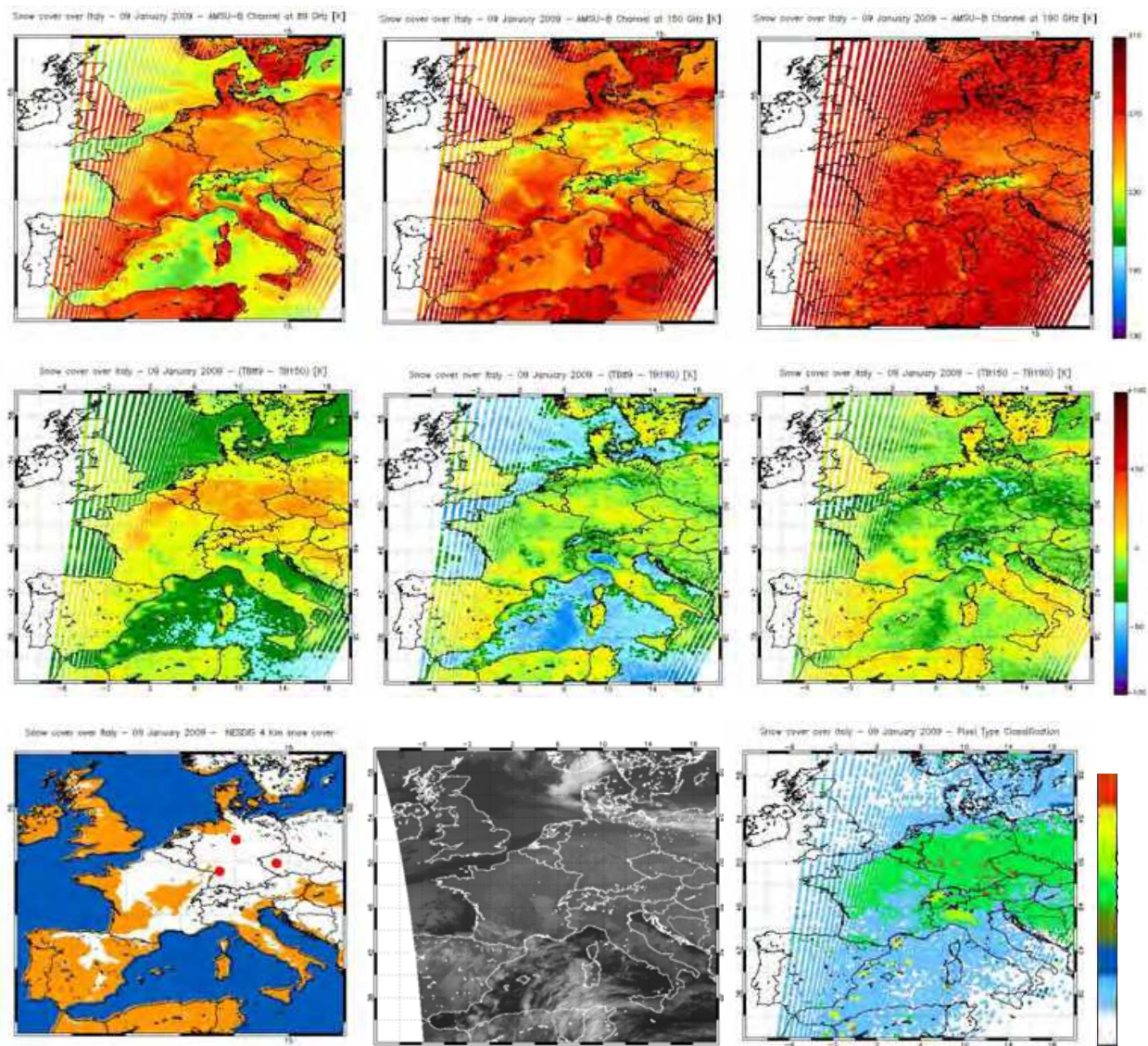


Fig. 1. NOAA-16 AMSU-B soundings on 09 January 2009, 0520 UTC, at 89 GHz (top-left), 150 GHz (top-middle) and 190 GHz (top-right), and corresponding MSG-SEVIRI image at $10.8 \mu\text{m}$ (bottom-middle). The snow cover pack is more clearly enhanced at 150 GHz with respect to other frequencies. Nevertheless, the combination of these frequencies can be used to detect snow. The snow mantle (bottom-left) is better highlighted with the threshold $(BT_{89} - BT_{150})$ (middle-left) but since the same values are quite similar to rainy ones the simultaneous application of tests based on $(BT_{89} - BT_{190})$ (middle-center) and $(BT_{150} - BT_{190})$ (middle-right) can be skillfully used to discern rainy from snow pixels. An example of snow cover map applied to the 183-WSL retrieval scheme is shown on bottom-right where green, Chartreuse green and lime-green are flags for snowfall, dry snow cover and wet snow cover, respectively; red and yellow dots refer to convective and stratiform precipitation; blue and cyan represent cloud liquid water and cloud droplets and finally white is the label for no-data.

2.2 The Radiative Transfer Equation

The radiative transfer equation is a mathematical description of the spatial-angular distribution of monochromatic radiation intensity I_ν which, at a certain instant t and at the frequency band ν , propagates into a medium across cross section A , in the observation direction Ω along the path s . The intensity of radiation varies while this passes through the medium. In particular, the energy of the incoming beam will decrease due to the absorption by the medium substance and to the deviation of a fraction of the radiation from the original trajectory due to the scattering in all directions. At the same time, the thermal radiation emission by the volume of material will enhance the energy balancing the net energy flux losses by the extinction processes. A brief phenomenological discussion on the radiation interaction properties with the material medium will be presented hereafter; the reader interested to a rigorous analysis should refer to more specialized books (e.g., Chandrasekhar, 1960). This general treatment of the properties of the energy interactions with matter, obtained by referring to the radiative transfer formulation discussed in Sharkov (2003), will allow us to readily focus on the practical scopes of this chapter by discussing the approximations of microwave radiative transfer and quantifying the extinction of the Earth's emission by natural disperse media such as clouds and rain observed from satellite in terms of brightness temperatures. Finally, the above theoretical and phenomenological concepts will be ideally combined in a method for the estimation of ground rainfall intensities through exploiting absorption and scattering mechanisms by hydrometeors.

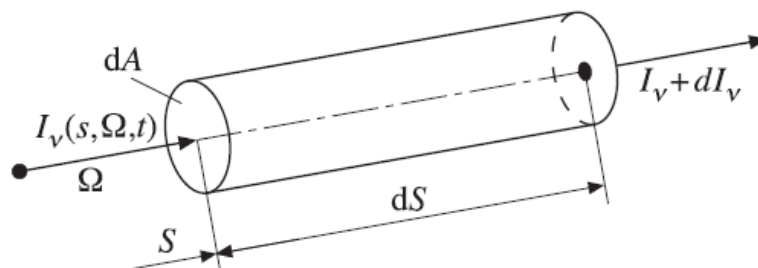


Fig. 2. Representation of the simple cylindrical geometry used to describe the total energy transformation from the initial intensity I_ν to the final $I_\nu + dI_\nu$.

If we consider an elementary volume $dAdS$ in the form of a cylinder with the main axis coincident with the radiation path s (Fig. 2), the variation of flux intensity when the incoming radiation passes through the elementary path ds is represented by the quantity:

$$dI_\nu(s, \Omega) dA d\Omega d\nu dt \quad (2.2.1)$$

where dA , $d\Omega$, $d\nu$ and dt correspond to elementary crossed surface, solid angle of energy propagation direction, frequency band in the vicinity of ν and unit of time, respectively.

Let us indicate with W the increase of the radiation I_ν passing through the above considered volume. The quantity

$$W_\nu dA ds d\Omega d\nu dt \quad (2.2.2)$$

represents the enhanced energy of an incident beam into the elementary cylindrical volume $dAds$ with respect to the direction Ω and relative to the time interval dt and frequency band dv . From the combination of the (2.2.1) and (2.2.2), the quantity W_v is derived in terms of the incoming intensity energy variation to unit path

$$\frac{dI_v(s, \Omega)}{ds} = W_v \quad (2.2.3)$$

By considering an absorbing, emitting and scattering medium, the quantity W_v can be written in the explicit formulation of interaction mechanisms as follows:

$$W_v = W_E - W_A + W_{IS} - W_{AS} \quad (2.2.4)$$

This relationship represents the balance equation between the increment (positive terms) and decrement (negative terms) of the energy during the interaction with material substance. In particular, the first term to right-hand side represents the increasing of radiation energy per unit time, volume, solid angle and frequency due to the emission of radiation, if the local thermodynamic equilibrium (LTE) is guaranteed and then the Kirckoff's law domain is established; it will be related to the Planck function and spectral absorption by following the relationship

$$W_E = \gamma_v(r) I_{vB}[\nu, T(r)] = \gamma_v(r) \left[\frac{2h\nu^3 n^2}{c_0^2} \frac{1}{\left[\exp(h\nu/kT) - 1 \right]} \right] \quad (2.2.5)$$

where $\gamma_v(r)$ characterizes the spectral absorption coefficient of the substance per unit of the radiation propagation path length, while the term in square brackets describes the Planck function in terms of frequency for a transparent substance with a refractive index n and temperature T . A strong approximation to linearly represent the Planck distribution is usually assumed in remote sensing practical applications at longer wavelengths (i.e., smaller frequencies) as in the radio-frequency regime. Derived by Rayleigh and Jeans, this reformulation of the Planck's formula can be achieved in the case where $h\nu/kT \ll 1$. After expanding in a Taylor series the exponential term of the black-body equation, the Rayleigh-Jeans radiation law can be obtained rewriting the (2.2.4) as

$$I_v(\nu, T) = \frac{2\nu^3 h}{c_0^2} \frac{1}{\left[\left(1 + \frac{h\nu}{kT} + \dots \right) - 1 \right]} \approx \frac{2\nu^2 n}{c_0^2} kT \quad (2.2.6)$$

This new formulation of Planck's law allows to directly calculate the radiative transfer in terms of brightness temperature (T_{BB}) linking the first term on the left-hand side to the properties of medium and its physical temperature on the right-hand side.

The second term of the (2.2.4) corresponds to the energy losses caused by the radiation absorption by a medium that, for a volume element in LTE and in the unit time, solid angle and frequency, can be written as

$$W_A = \gamma_v(s) I_v[s, \Omega] \quad (2.2.7)$$

The third and fourth terms describe the balance of radiation energy diffused in all direction by the scattering mechanisms. Specifically, the quantity W_{IS} takes into account the radiation scattered by the medium in the direction of the observer (positive) that, for an isotropic medium and purely coherent scattering, can be expressed as

$$W_{IS} = \frac{1}{4\pi} \sigma_v(s) \iint_{4\pi} I_v(s, \Omega') p_v(\Omega') d\Omega' \quad (2.2.8)$$

while the quantity W_{AS} is related to radiation losses for the reason that the energy beams are deflected along the main direction Ω . In terms of the unit of time, volume, solid angle and frequency, it can describe by the following equation

$$W_{AS} = \sigma_v(s) I_v[s, \Omega] \quad (2.2.9)$$

where the quantities $\sigma_v(s)$ and $p_v(\Omega')$ represent the spectral scattering coefficient and spectral phase function normalized to unit, respectively. By substituting the explicit relationships into the compact formulation (2.2.4), we have

$$\begin{aligned} \frac{dI_v(s, \Omega)}{ds} + [\gamma_v(s) + \sigma_v(s)] I_v(s, \Omega) &= \\ = \gamma_v(s) I_{vB}[T(s)] + \frac{1}{4\pi} \sigma_v(s) \iint_{\Omega'=4\pi} I_v(s, \Omega') p_v(\Omega') d\Omega' \end{aligned} \quad (2.2.10)$$

that, in more compact form, could be written as

$$\frac{1}{\beta_v(s)} \frac{dI_v(s, \Omega)}{ds} + I_v(s, \Omega) = S_v(s) \quad (2.2.11)$$

where

$$S_v(s) = (1 - \omega_v) I_{vB}[T(s)] + \frac{1}{4\pi} \sigma_v(s) \iint_{\Omega'=4\pi} I_v(s, \Omega') p_v(\Omega') d\Omega' \quad (2.2.12)$$

$$\beta_v(s) = \gamma_v(s) + \sigma_v(s) \quad (2.2.13)$$

$$\omega_\nu = \frac{\sigma_\nu(s)}{\gamma_\nu(s) + \sigma_\nu(s)} \quad (2.2.14)$$

In these relations $S_\nu(s)$ is called the source function, $\beta_\nu(s)$ is the spectral extinction coefficient and $\omega_\nu(s)$ is the spectral albedo.

In the following part two useful examples will be proposed to better elucidate the theoretical concepts expressed above. In particular, the complete equation (2.2.10) will be specialized for particular cases of a purely scattering medium and of a solely absorbing and emitting medium and each of them will be described with the help of real satellite images. Nevertheless, it is essential to clarify that the cases to which the satellite images refer in the example are quite close to the ideal cases of the theoretical description of the atmospheric extinction processes and simply represent a rough fitting of the theory. Many aspects predicted by the theory are neglected on purpose to simplify the treatment and concentrate the interests to the core of the problem.

If we observe a hypothetical real purely scattering medium, namely where the thermal radiation does neither absorb nor emit such is the case of the frozen top of cold rainy clouds, equation (2.2.14) will be banally simplified as $\omega_\nu(s) = 1$. With this simplification, the term related to Planck's emission in equation (2.2.12) completely disappears and the total extinction coefficient (2.2.13) becomes $\beta_\nu(s) = \sigma_\nu(s)$. Equation (2.2.14) can be rewritten as:

$$\frac{1}{\sigma_\nu(s)} \frac{dI_\nu(s, \Omega)}{ds} + I_\nu(s, \Omega) = \frac{1}{4\pi} \sigma_\nu(s) \iint_{\Omega'=4\pi} T_\nu(s, \Omega') p_\nu(\Omega') d\Omega' \quad (2.2.11-a)$$

This is an integro-differential equation and its analytical solution does not exist. Several methods often based on approximated formulation of the (2.2.11) could be found in more specialized books.

On the other hand, absorbing and emitting media differ from purely scattering ones because they absorb external radiation and re-emit it in the same direction without scattering extinction by the substance constituents. Small cloud droplets, water vapor and precipitating clouds with few ice crystals on top or totally deprived of them (warm rain) can be virtually considered as an absorbing/emitting medium. For such media, where $\omega_\nu(s) = 0$, the equation (2.2.11) assumes the form:

$$\frac{1}{\beta_\nu(s)} \frac{dI_\nu(s, \Omega)}{ds} + I_\nu(s, \Omega) = I_{\nu B} [T(s)] \quad (2.2.11-b1)$$

That, solved in terms of radiation energy intensity, becomes

$$I_\nu(s, \Omega) = I_0 \exp(-\beta s) + \int_0^s I_{\nu B} [T(s')] \exp(-\beta s') ds' \quad (2.2.11-b2)$$

where the first term represents the amount of absorption of external radiation by the medium described by the boundary intensity radiation I_0 and an exponential decreasing law of incoming radiation into the medium; the integral term expresses the radiation variation emitted from the surface at the temperature T along the path length s .

In order to show the effect of scattering and absorption on a real satellite measurement it can be useful to consider the images in Fig. 3 and 4. Specifically, those images refer to the soundings at high frequencies of the AMSU-B PMW sensor. Considering that AMSU-B channels are ranged in the scattering domain (generally scattering effects increase for $\nu > 60$ GHz whereas for $\nu < 60$ GHz the radiation extinction is conventionally attributed to the absorption processes), many sensitivity studies (Bennartz & Bauer, 2003) have demonstrated that in absence of strong scatterers liquid cloud droplets largely absorb radiation at 89 GHz while ice hydrometeors on the top of clouds act as scatterers more at 150 GHz and 190 GHz than at the other frequencies. Furthermore, our experiments demonstrate that when a light precipitation episode is sensed, usually associated to stratiform rain with raindrop sizes comparable to non-rainy cloud droplets, the sensitivity to the absorption at 89 GHz is more marked than the scattering signal at 150 GHz. Therefore, making use of these basic considerations we report an example of intense scattering by large ice crystals during the evolutionary stages of a Mesoscale Convective System (MCS) over the Mediterranean Sea and an example of absorption by light stratiform rain and cloud liquid water over the North-Eastern England Sea.

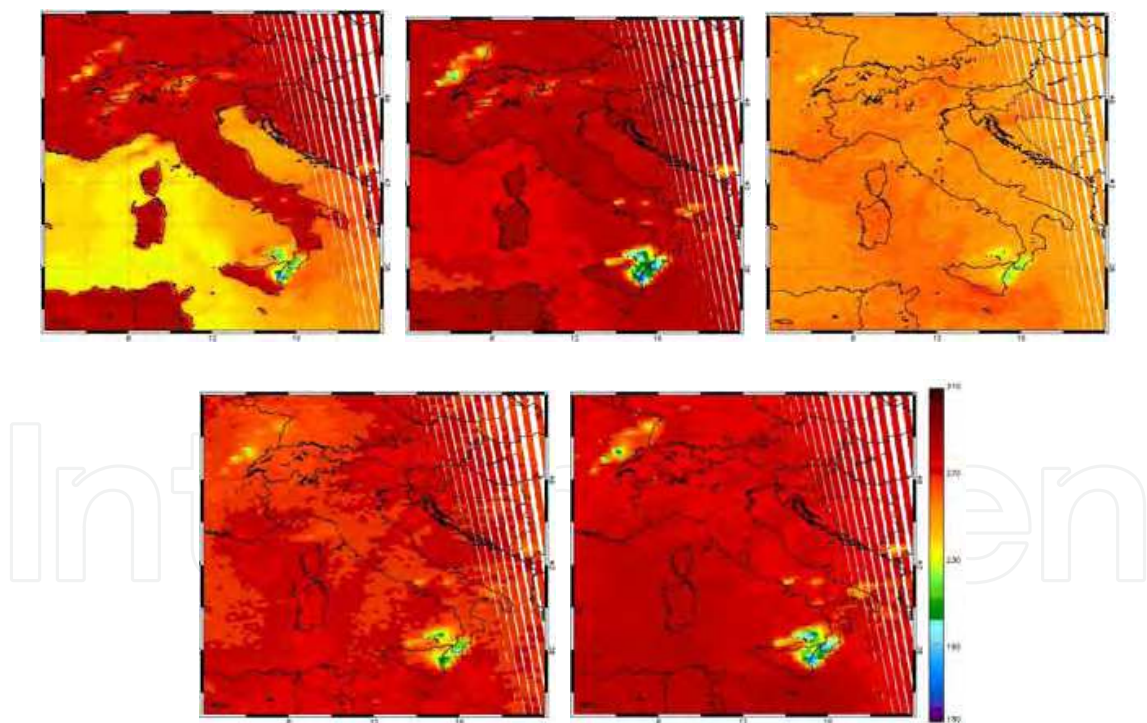


Fig. 3. Mesoscale Convective System over Southern Italy on 22 October 2005 as observed by the NOAA-15/ AMSU-B at 89 , 150 , 184, 186 and 190 GHz anticlockwise from top left panel. Neglecting a small radiation absorption by surrounding droplets and water vapor molecules more evident at the opaque frequencies, the convective region can be considered as a purely scattering medium. At 150 GHz the brightness temperature depression was registered above 100 K with respect to its nominal value.

In the case of deep convection it is worth noting how the ice particle bulk depresses upwelling radiances, expressed as brightness temperatures in unit of Kelvin, at all frequencies from surface (89 GHz and 150 GHz) to the top of the troposphere (at 184 GHz the weighting function “peaks” at about 8 km lowering down to 2 km at 190 GHz) denouncing a system vertically well developed.

Besides, it is interesting observe that the signal depression is enhanced at 150 GHz (comparable with measurement at 190 GHz) where the signal extinction is quantifiable over 100 K with respect to the channel’s nominal value. In the practical use of satellite remote sensing, the properties of this frequency combined to those of other channels such as the 89 GHz and 190 GHz are often exploited to discern ice signature in the clouds and possibly correlate probability information related to the conversion of melting ice into rainfall at the ground (Bennartz et al., 2002; Laviola & Levizzani, 2008).

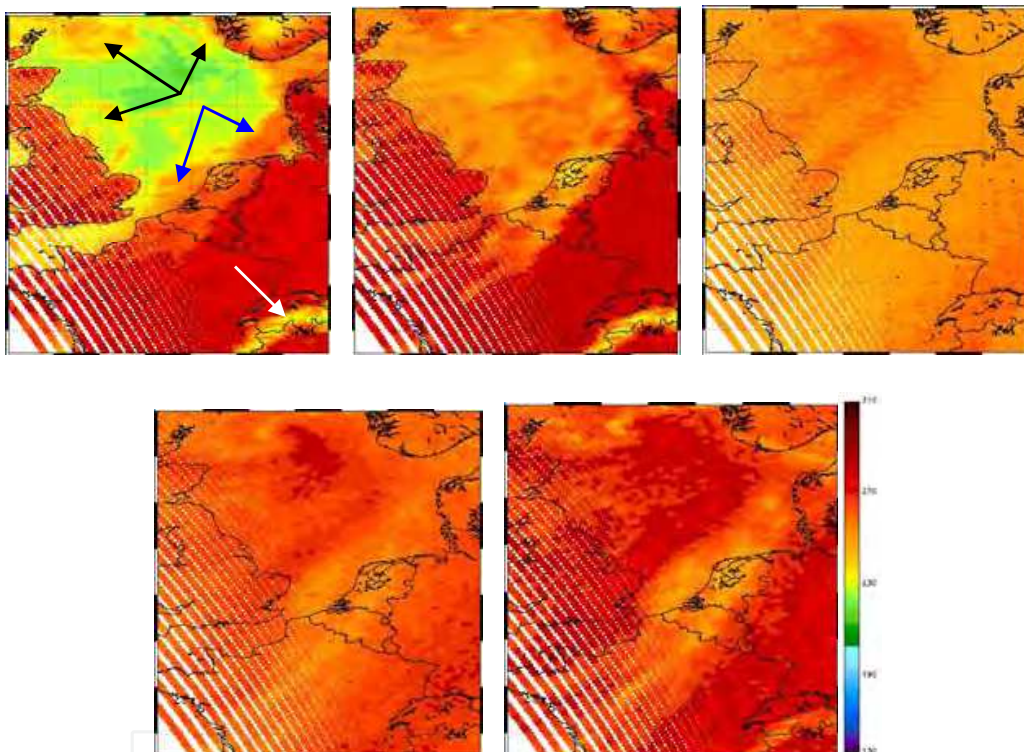


Fig. 4. Quasi-pure stratiform system over Belgium and cloud liquid water over North-Eastern England Sea on 17 January 2007 as observed by the NOAA-15/AMSU-B at 89 , 150, 184, 186 and 190 GHz anticlockwise from top left panel. The strong contrast at 89 GHz allows to observe water clouds over open sea (black arrows) whereas the change in emissivity highlights snow cover over Alps both at 89 and 150 GHz (also at 190 GHz). At higher opaque frequencies (186 and 184 GHz) the absorption of middle and high layer water vapor can only detected.

Referring to Fig. 4, the observed satellite radiance attenuation is mainly due to the absorption and emission of small cloud particles and hydrometeors. Nevertheless, a more realistic description of the situation would have to take into account that the variation of upwelling radiation is certainly due to the combination of absorption and scattering by a mixture of liquid and ice hydrometeors and disperse liquid particles. By the same token, in

the previous cases the absorption due to water vapor and small cloud droplets, which typically surround precipitating clouds as a halo, was not considered because it is small enough with respect to scattering of radiation by ice crystals on cloud top.

Referring once more to the case of Fig. 4, warm cloud spots at 89 GHz due to the absorption of water clouds over open water (black arrows) and stratiform rainy clouds (blue arrow) over the coastline also sounded at 150 and 190 GHz can be clearly distinguished. It is interesting to compare extinction intensities at 89 and 150 GHz both from the absorption and scattering point of view by using in that order open sea liquid cloud and snow cover over the Alps (white arrow) as terms of comparison. At 89 GHz over the sea the strong contrast between cold sea surface (≈ 200 K) and warmer liquid clouds (≈ 250) bring to a net difference of about 50 K whereas over land the difference due to the scattering of snowy terrain is quantified in about 60-70 K. At 150 GHz the discrepancy between the cold sea surface and liquid water clouds can be evaluated in about 10 K while the change in surface emissivity over land induces a satellite brightness temperature depression up to 70 K increasingly describing the strong sensitivity of that frequency to the scattering.

3. Impact of precipitation on microwave measurements

In the approximation of disperse media theory, natural systems such as dust, fog, clouds, rain particles are considered as heterogeneous polydisperse media consisting of mixtures of substances and/or different thermodynamic phases. Assuming a particle size density function $n(r)$ described by the M-P function (Marshall & Palmer, 1948) and a drop terminal velocity $V(r)$ depending on particle radius r , rainfall rates will be proportional to the fourth or third moment of the drop density function. From the radiative point of view, when incident radiation interacts with precipitating hydrometeors all particles present in any elementary volume are totally irradiated and consequently the incoming radiation is extinguished both by absorption and scattering processes at the same time.

Passive microwave rainfall estimations are carried out by exploiting either absorbed or scattered signals from raindrops or a combination of the two as is the case of the 183-WSL method. In the hypothesis of warm rain rainfall is estimated through the emission associated with absorption by liquid hydrometeors through Kirchoff's law. In this case, raindrops absorption and emission provide a direct physical relationship between rainfall and the measured microwave radiances. With increasing precipitation intensities, scattering by large drops becomes dominant with respect to absorption and the observed radiation appears drastically depressed for a downward-viewing observer.

A more realistic situation is represented by rainclouds formed by a mixture of liquid, frozen and eventually supercooled hydrometeors. Since scattering is primarily caused by ice hydrometeors aloft the emitted signal by liquid drops is substantially blocked by intense scattering and its contribution to the total extinction significantly decreases with the increase of the frozen bulk. Measured radiances are therefore indirectly related to the rain mass and consequently the estimations become less correlated with falling rain below cloud base.

This situation is often observed during the development of intense convections (see Fig. 3) typically associated with heavy rain events. The case of liquid rain drops discussed before can be roughly associated with the stratiform systems (see Fig. 4) whose light precipitation is linked more to the absorption of water droplets than to the scattering of small crystals which form on cloud top.

This theoretical argument associated with the treatments of previous paragraphs is useful to understand the behavior of the 183-WSL with respect to condensing water vapor. When the newly nucleated droplets surround a developing rainy region, they can act as embryos for the development of small rain drops. Depending on the updraft strength such droplets can be dragged inside the cloud core thus contributing to the cloud's precipitation formation mechanisms or can freely evolve into light rain constrained to the border of the main cloud body. The small size of the buoyant drops in these bordering areas determines the signal extinction, particularly at 183.31 GHz, to be characterized by absorption rather than by scattering.

4. High frequency method to retrieve rainrates

A new rainfall estimation method, named 183-WSL (Laviola & Levizzani, 2008, 2009a), is now described based on the high frequency water vapor absorption bands at 183.31 GHz of AMSU-B sensors on board NOAA and EUMETSAT Polar System (EPS) satellites, which is conceived to retrieve rainrates over land and sea. AMSU-B is the second module of the AMSU passive MW across-track scanner operating into the frequency range from 90 up to 190 GHz with a spatial resolution of 16 km at nadir view (Saunders et al., 1995; Hewison & Saunders 1996).

An emission approach at 183.31 GHz is adopted to infer surface precipitation because one of our major targets is the estimation of warm rain. The 183-WSL retrieval scheme (Laviola & Levizzani, 2009b), based on a suite of brightness temperature (BT) thresholds, distinguishes and classifies convective and stratiform precipitation while filtering out condensed water vapor and snow cover on mountain top, which particularly affects more opaque superficial channels (i.e., 190 GHz).

4.1 The sensitivity at 183.31 GHz to surface emissivity and rainy cloud altitudes

The 183.31 GHz bands are mainly dedicated to the sounding of the atmospheric water vapor amount (Kakar, 1983; Wang et al., 1989). However, several studies have demonstrated the effects of clouds on these frequencies and their possible application into rainfall retrieval schemes. Note that the use of PMW information is necessary to detect rainy systems or correct and integrate IR measurements, for instance in the blended techniques. However, their use is limited because of the variability of surface emissivity (ϵ). Grody et al. (2000) proposed a few algorithms based on different land type studies to evaluate surface emissivity using AMSU data.

Here we choose radiative transfer results with different values of surface emissivity, which refers to land if ϵ is typically > 0.6 and to water in the other cases, to quantify the effect of surface on AMSU-B channels.

Fig. 5 shows the simulated brightness temperatures for all AMSU-B frequencies as a function of surface emissivity in clear sky conditions. The results are obtained by a adding/doubling radiative transfer model (Evans et al., 1995a,b) running with mid-latitude profiles and coupled to Rosenkranz (2001) approach for the computation of the absorption at selected frequencies.

As expected, the signal around 89 and 150 GHz has strong surface contributions showing a deep depression near low emissivity values and converging about to the same brightness temperature when $\epsilon=1$ (dry-land). Therefore, the decreasing surface emissivity from dry-

land values to water bodies' enhances the influence of atmospheric moisture on these channels. Another significant aspects of Fig. 6 is that, since their weighting functions are peaked beyond 2 km altitude, the three moisture channels are little or not at all affected by different surface emissivities thus suggesting their application both over land and over the sea.

Effect of Surface Emissivity on AMSU-B Frequencies (Mid-Latitude)

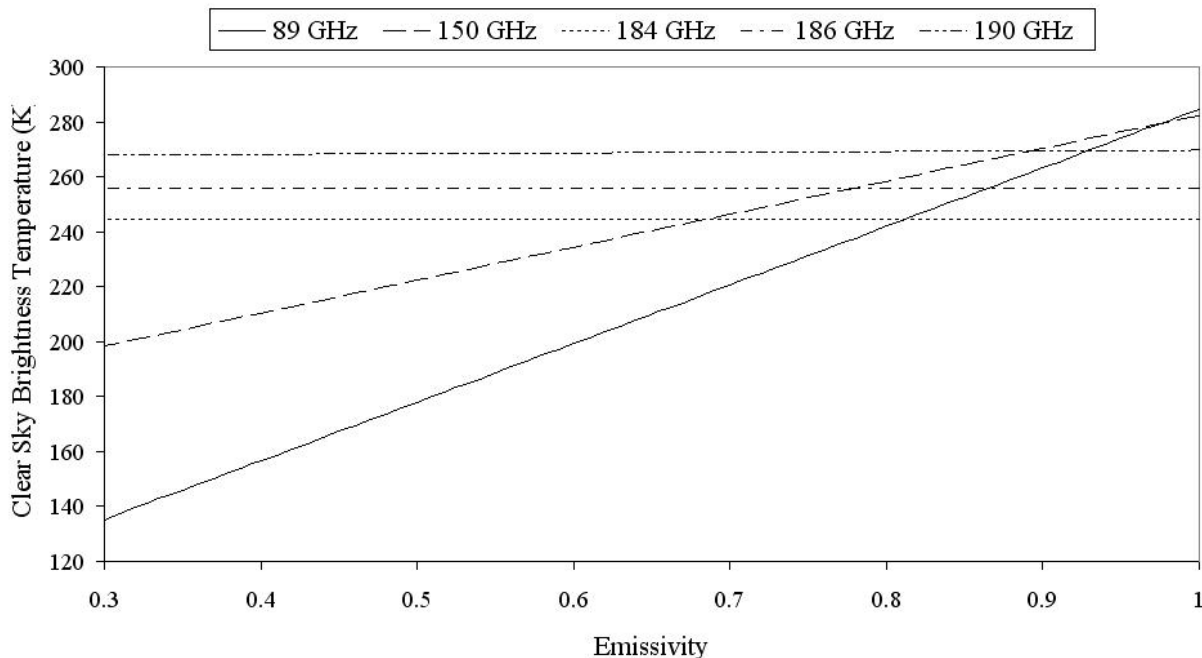


Fig. 5. Emissivity effects on the AMSU-B channels. The two window channels are strongly dependent on the surface emissivity showing an increasing value up to 280 K from the simulated sea surface ($\epsilon = 0.50$) to dry land ($\epsilon = 1.00$). At moisture frequencies, where the weighting functions are higher than window ones, the surface emissivity effect is low.

Other sensitivity studies not reported here have emphasized that, when moving towards higher latitudes where the atmosphere is less optically thick, the contribution of surface emissivity affects more and more the measurement particularly at 190 GHz where also thinner ice clouds can modify the signal.

Precipitating cloud altitude is another important variable affecting the AMSU-B brightness temperatures. We studied the behavior of AMSU-B moisture channels as a function of the position of a rainy cloud in the troposphere. All simulations have been carried out using radiosonde temperature and humidity profiles screening out the possible cloud formations along balloon trajectory with the threshold suggested by Karstens et al. (1994). The cloud structure is built adopting a Marshall-Palmer's water drop size distribution (Marshall & Palmer, 1948) and the Mie theory to solve the scattering equations. In agreement with the weighting function distribution, which peak between 2 and 8 km, our results show that only rainy clouds positioned above 2 km altitude interact with three AMSU-B opaque frequencies at 183.31 GHz and the interaction will be always more intense as the cloud becomes thicker.

4.2 Physical basis of the 183-WSL algorithm

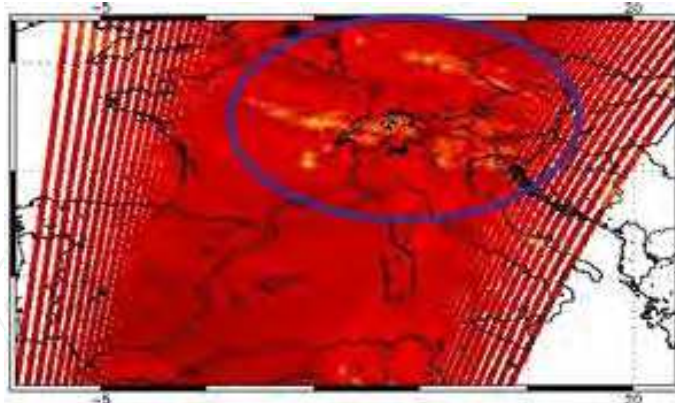


Fig. 6. 11 June 2007, 0957 UTC. NOAA/AMSU-B 183.317 GHz brightness temperatures of a stratiform system over France. The blue circle contains the detected low rainrate clouds.

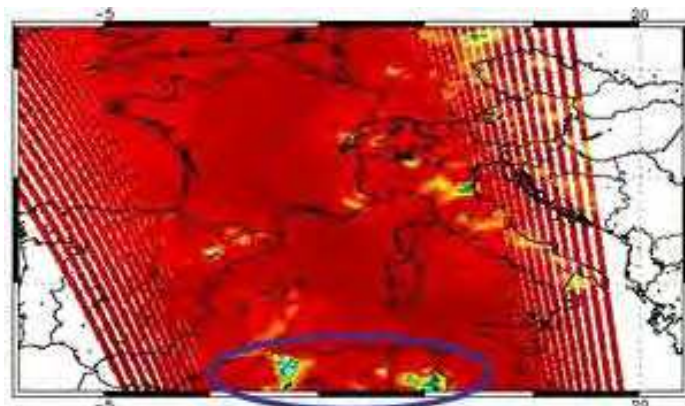


Fig. 7. 12 June 2007, 1457 UTC. NOAA/AMSU-B 183.317 GHz brightness temperatures of a deep convective system over the coast of North Africa. The blue circle contains the two convective cores.

A substantial number of precipitating systems forming in the lower atmospheric layers at mid latitudes are formed for the large portion by water drops grown through the collision and coalescence mechanism because cloud temperature does not reach values low enough for the droplets to start freezing. This implies that the vertical rain profile is a few km thick and that falling rain will presumably be light and persistent.

On the other hand, strong updrafts typical of the warm season are capable of transporting water drops up to the tropopause level giving rise to deep convective columns, which convey a large amount of cloud water to the ground through heavy showers. These two kinds of precipitation systems induce very different BT responses in the MW spectral range as observed in Fig. 6 and 7 where the soundings of a stratiform and of a convective system at 183.31 ± 7 GHz are shown, respectively. In the first, low rain clouds absorb the Earth radiation showing a moderate cold area corresponding to BTs in the 240-250 K range. The second situation refers to a deep convective system over Africa consisting of two cores, which strongly depress the BT reading of the instrument (≈ 200 K) because of the scattering of large ice crystal located at cloud top.

The 183-WSL algorithm is based on a linear combination of the AMSU-B opaque channels and it detects rainrates (in mm h⁻¹) over land and sea by sounding cloud features from 1-2 km up to the top of the troposphere according to the channels weighting functions. Note that, however, since our studies have shown that when a light-rain stratiform system forms large amounts of the surrounding water vapor absorbs the 183 GHz radiation inducing false rain signals, a suite of thresholds is introduced to reduce these spurious effects (see Table I). In addition, tests carried out during the winter season highlight that the scattering signal at 183.31 ± 7 GHz relative to the snow cover on mountain top (the Alps in this case) is comparable to the ice scattering signature at the top of convective cloud.

Classification	Land (K)	Sea (K)
Water vapor/Snow cover	$\Delta T < 3$	$\Delta T < 0$
Stratiform rain	$3 < \Delta T < 10$	$0 < \Delta T < 10$
Convective rain	$\Delta T > 10$	$\Delta T > 10$

Table 1. Classification thresholds based on the window channel differences $\Delta T = (T_{89} - T_{150})$

4.3 The 183-WSL algorithm: retrieval design and performances

The 183-WSL work design is schematically described by four steps. The first step is dedicated to ingesting and processing the satellite data stream. All relevant information, namely BTs, surface type (land/sea/mixed), satellite local zenith angles, topography, are separated from the overall data stream and arranged for input into the 183-WSL processing chain. The second and third steps are constituted by the modules 183-WSLW and 183-WSLS/C, respectively, which operate to discriminate rainy from non rainy pixels and classify precipitation type as a stratiform or convective on the basis of threshold values calculated for land/mixed and sea surfaces. This step is currently been improved adding a new module to classify cloud liquid water by estimating the amount of water in terms of the Liquid Water Path (183-LWP) and with a snow cover mask able to recognize snowy soils and categorize those pixels as wet or dry snow. These improvements (not included in the 183-WSL version used for the examples of this chapter) were needed to reduce the number of false rain signals especially during winter season when also snowy terrain deeply scatter the upwelling radiation similarly to ice hydrometeor signatures. Finally, the last step of the 183-WSL algorithm computes the final rainrate product in unit of mm h⁻¹.

The proposed case studies exemplify different situations in which rainfall was retrieved and classified by means of the two 183-WSL convective/stratiform modules (183-WSLC/S). In the first case the values of the scattering index (SI) introduced by Bennartz et al. (2002) to build four rain intensity classes were used for comparison. As expected, the agreement between the SI and the 183-WSLC (convective) is higher than the one between the SI and the 183-WSLS (stratiform). The reason refers to the nature of the SI that retrieves only the probabilities of surface rainrates due to melting of scattering ice crystals. Therefore, the scattergrams related to the stratiform portion and to water vapor should be intended as light-rain low-SI values. At the same time the water vapor distribution threshold based on the BT differences between 89 and 150 GHz should be < 0 K (sea) and < 3 K (land).

The other two cases show a comparison between the 183-WSL and retrievals of the Goddard Profiling (GPROF) algorithm (Kummerow et al., 1996, 2001). A good agreement is found particularly in the case of intense rainfall. When ice crystals form during deep convective rain development the increase of scattered radiation is better observed by both algorithms with respect to the case of extinction caused by light rain, for which the 183-WSL algorithm shows more sensitivity than GPROF.

4.3.1 Saharan dust causing red rain over Bulgaria

On 23 and 24 May 2008 an intense dust plume from Sahara overflying Greece and the Black Sea interacted with an Atlantic Front generating persistent “red” rain over Bulgaria (Fig. 8, white arrows). The strongly scattering but non-precipitating hydrometeors (water vapor around dust over the Mediterranean Sea) are filtered out by the computational scheme (8-f). The incoming Atlantic front generates deep convection over Italy with rainrate estimations around 10 mm h^{-1} . Note that the classification thresholds correctly flag as precipitating those pixels where BTs are greater than 3 K (8-a) as compared with the MODIS-COT (Moderate Resolution Imaging Spectroradiometer-Cloud Optical Thickness) product shown in 8-b. Rain classification in Fig. 9 (left) shows that the 183-WSL low rainrates ($< 5 \text{ mm h}^{-1}$) are associated with scattering signatures (Bennartz et al., 2002) $< 30 \text{ K}$ whereas rainrates classified as heavy ($> 5 \text{ mm h}^{-1}$) are correlated with the highest SI values. On the middle and right of Fig. 9, rain distribution with longitudes and rain types on the basis of classification thresholds are respectively proposed.

4.3.2 Severe storm over Italy: 183-WSL vs GPROF/AMSR-E

During the severe storm of June 2007 we have tested the 183-WSL performances both in the convective portion and in moderate rain conditions that characterized the various sectors of the storm, with light rain being not very frequent. The 183-WSL underestimates rainfall with respect to GPROF/AMSR-E. From the analysis of the discrepancy graphs (vertical bars) an increasing displacement is noted with increasing rain intensities. This is possibly due to the different nature of the algorithms. In the case of moderate rain (Fig. 10-a) the precipitating areas are quite similar over the southern Mediterranean Sea; over the northern sector GPROF drastically underestimates and this is true for the other cases. Note that the convective system coming from SE (Fig. 10-b) is well described but 183-WSL precipitation presents a more continuous pattern from the convective core to the borders. In case of lighter rain (Fig. 10-c) the 183-WSL captures more rainy areas than GPROF/AMSR-E, especially over the Alps.

4.3.3 Hurricane Dean: 183-WSL vs GPROF/TMI

Cyclone Dean was a classic seasonal tropical system forming over the Cape Verde islands, passing close to Jamaica and pouring rain on the coast of the Yucatan as a category 5 hurricane. Figure 11 shows the cyclone development stages retrieved by the 183-WSL algorithm (top) and TRMM 2A12 product from the best coincident overpasses (bottom). By comparing the TMI and the 183-WSL products a reasonable agreement can be observed although a more comprehensive study needs to be carried out.

The scattergrams at the bottom of Fig. 11 depict a generally good correlation between the two retrieval techniques. Nevertheless, some other studies of ours describe a slight

overestimation of the 183-WSL but this is probably due to the large water vapor absorption characteristic of this kind of extreme event.

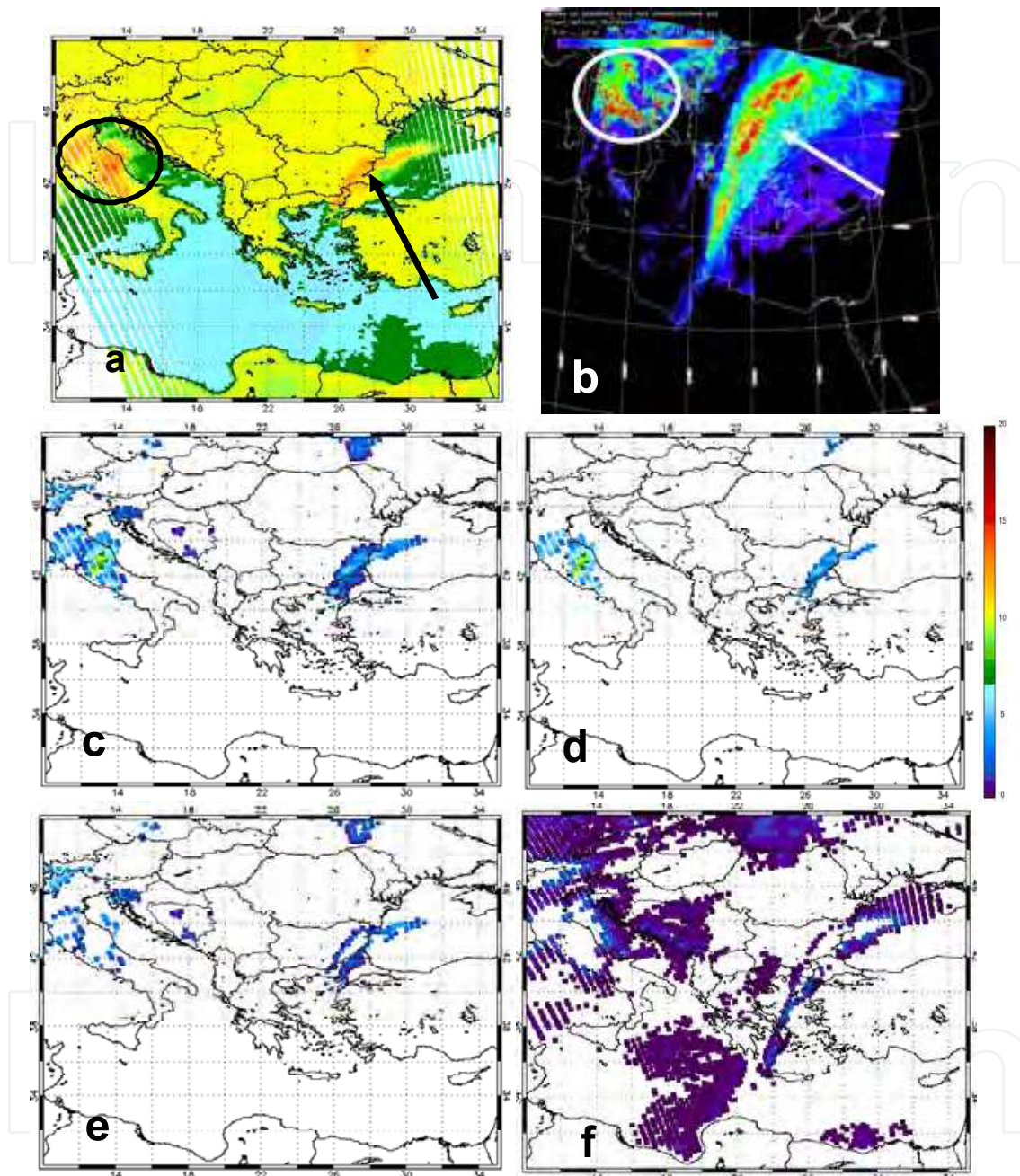


Fig. 8. "Red rain" over Bulgaria on 23 March 2008 0920 UTC. The classification thresholds (a) correctly discriminates between rainy areas, generally characterized by high values of Cloud Optical Thickness (MODIS-COT in b), from non-rainy. From (c) to (f): 183-WSL rainrate estimations, 183-WSL convective rain, 183-WSL stratiform rain and 183-WSL condensed water vapor removed from the computations.

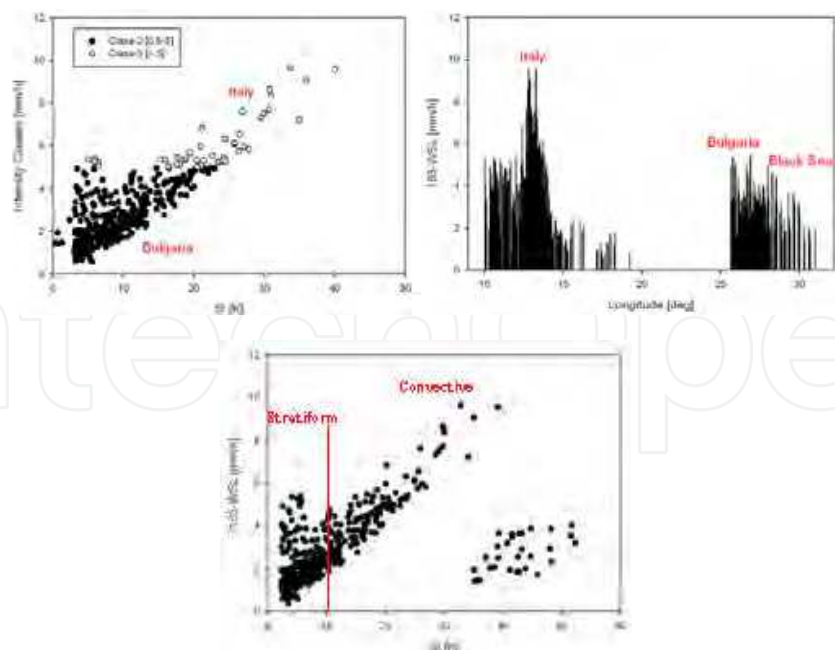


Fig. 9. Scattergrams of the case study in Fig. 8. In figure left, a comparison between classified 183-WSL rain intensities in class 1 [0-5 mm h⁻¹] and class 2 [> 5 mm h⁻¹] and the scattering index (SI) values is shown. Note that rainfall intensities belonging to class are associated to lower SI values (SI < 30 K) whereas rainrates > 5 mm h⁻¹ correspond to SI values around 50 K. Figures middle and right describe rainfall distribution with latitude and rain types, respectively.

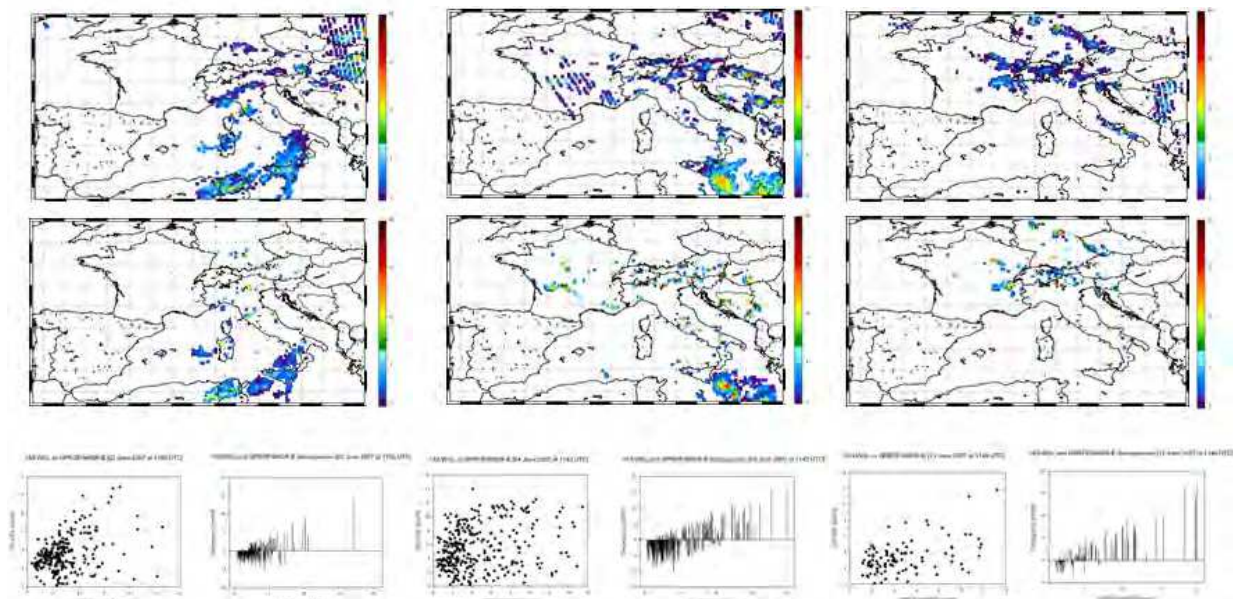


Fig. 10. Severe storm over Italy on 2 June 1156 UTC (left), 4 June 1143 UTC (middle) and 11 June 1149 UTC (right). The 183-WSL rainrates (top) are compared with those from GPROF/AMSR-E (bottom). Vertical bars describe an increasing displacement of the 183-WSL estimations with increasing rain intensities. The large dispersion of the scattergrams can be justified observing that GPROF drastically underestimates rain intensities where light rainfall is detected.

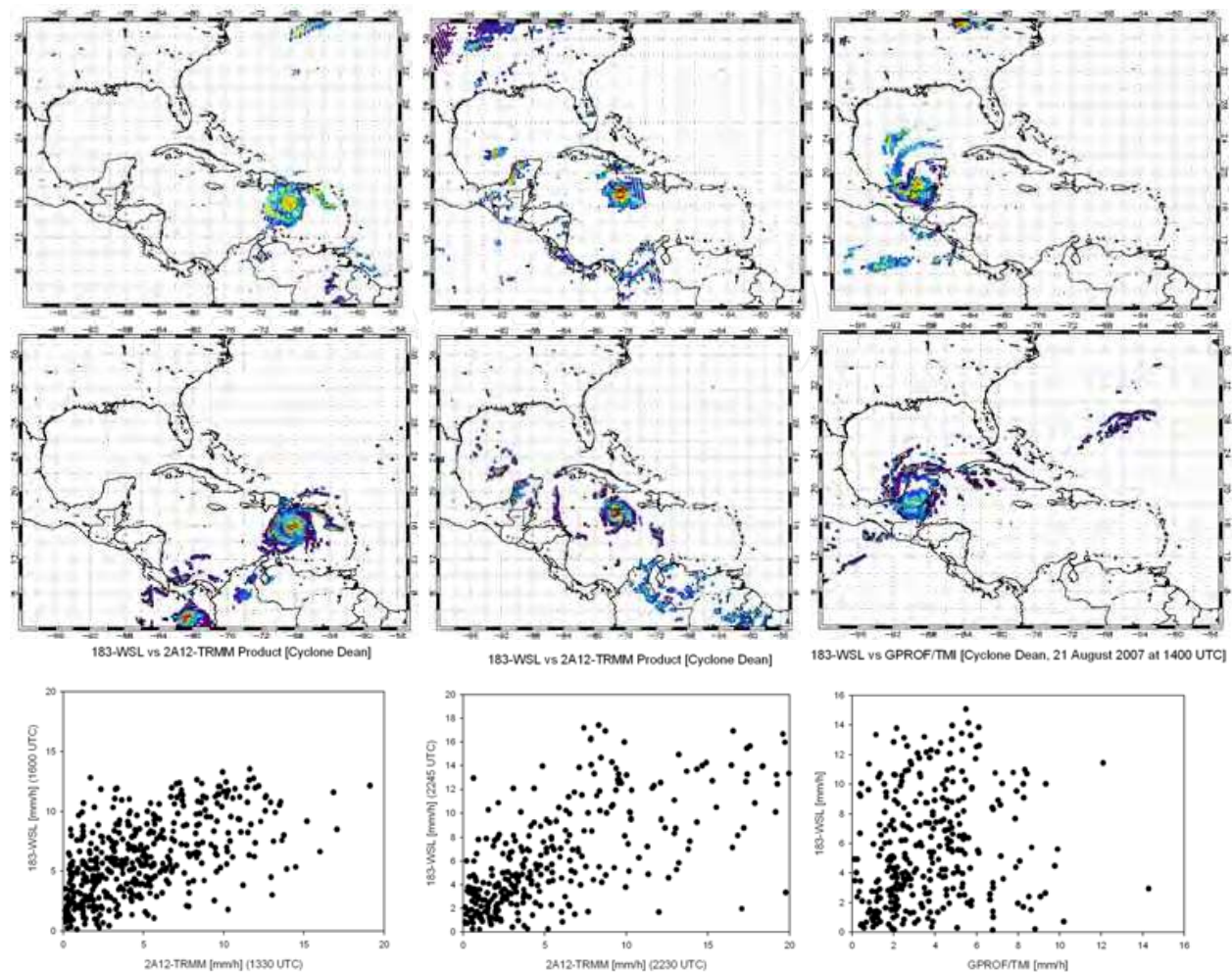


Fig. 11. Cyclone Dean, 18-21 August 2008. The 183-WSL retrievals (top) and corresponding TRMM 2A12 product images on 18 at 1300 UTC, 19 at 2200 UTC and 21 at 1400 UTC, respectively. Diagrams clearly show the increasing of correlation between the 183-WSL and TRMM 2A12 to increase of rain rates.

5. Summary and conclusion

The most important aspects of passive microwave remote sensing has been explored both from theoretical and for operational point of view. The chapter does not rigorously treat the physical principles of PMW remote sensing, but uses theory as a reference point to correctly interpret and describe satellite observations. For this reason, the first sections were contributed to focus the attention on two fundamental themes that must be taken into account when using microwave radiometers: surface emissivity and radiation extinction processes. Compared to optical and IR wavelengths where surface contribution varies between $0.80 \div 1.00$, microwaves are very susceptible to changes in surface conditions. Over ocean, the substantially stable emissive surface ensures that microwave soundings of atmospheric parameters are quite consistent within a strategy of rainrate retrieval. Over land areas, the passive microwave observations yield to significantly less quantitative measures of rainfall because the effects of surface emission variability can drastically affect measurements and consequently the retrieved products. Those surface effects are more marked in the case of

absorption by liquid raindrops where a low-emissivity background (i.e. cold) is required in order to make observations of the emitted radiation associated through Kirchhoff's law to the absorption regime. Liquid hydrometeors are the dominant contributors to the absorption and emission, providing a direct physical relationship between rainfall and the observed microwave radiances. Examples of the quasi-pure absorption process can be found in the Tropics where the dissolving of a deep convection system induces the development of stratified warm precipitation where collision-coalescence formation mechanisms accrete raindrops.

In the case of scattering, rainfall amount is indirectly estimated via the scattering of radiation by liquid and ice particles. Because scattering is mainly due to frozen hydrometeors located on the top of clouds, the ice pack aloft largely blocks emission by liquid raindrops below. Consequently, the upwelling radiation is not directly correlated to the bulk of rain and rainfall intensity is deduced as a result of an effective measure of the radiation-raindrops interaction but as a probability function of scattered radiation-rainfall. Retrieval methods based on scattering approach, however, allow for the observation of precipitation over any background with the limits of being very robust during rain events characterized by large amount of ice crystals on cloud top (see the MCS in Fig. 3) and almost "blind" during rain episodes where less or no-ice particles are formed (i.e., light stratiform rain or warm rain).

To practically discuss the differences of retrieval techniques based on absorption or scattering approaches we have proposed in the second part of the chapter the results of the algorithm 183-WSL, which basically works via absorption mechanisms but behaves increasingly similarly to scattering algorithms with the increment of ice aggregates in the cloud. The scattergrams in Fig. 9 quantitatively demonstrate that for rainrates belonging to the light-moderate intensity class the distribution is quite disperse indicating low correlation between the 183-WSL retrievals and co-located scattering index (SI) values. With increasing rainfall intensities the agreement 183-WSL-SI improves (see empty dots). Another example is shown in Fig. 10 where low rainfall intensity values are observed and numerically quantified by vertical bar diagrams.

These case studies on one hand highlight the differences between two retrieval methods based on absorption and substantially pure scattering processes and from the other they open up the road to future planned studies. Our numerous investigations actually reveal the robustness of the 183-WSL algorithm in many different situations where precipitating events are often characterized by light rains or snow covered terrain, two extreme circumstances for passive microwave observations. The strength of such results can be extended to a more general discussion on the use of high frequency microwaves to better delineate low rainrate regions and to inspect frozen soils. In addition, our studies also demonstrate that the suite of frequencies between 90 and 190 GHz, are suitable to study rainfalls mainly resulting from non ice-phase process with size spectral range lower than millimeter where these frequencies offer useful information to identify and possibly measure "warm rain" processes.

6. References

- Banghua, Y.; Weng, F., & Meng, H. (2008). Retrieval of snow surface microwave emissivity from the advanced microwave sounding unit, *J. Geophys. Res.*, 113, D19206, doi:10.1329/2007JD009559, pp. 1-23.

- Bennartz, R. & Bauer P. (2003). Sensitivity of microwave radiances at 85–183 GHz to precipitating ice particles, *Radio Sci.*, 38(4), 8075, doi:10.1029/2002RS002626.
- Bennartz, R., Thoss A., Dybbroe, A., & Michelson D. (2002). Precipitation analysis using the Advanced Microwave Sounding Unit in support of nowcasting applications, *Meteorol. Appl.*, 9, pp. 177-189.
- Cattani, E., Melani, S., Levizzani, V., & Costa, M. J. (2007). The retrieval of cloud top properties using VIS-IR channels. *Measuring precipitation from space - EURAINSAT and the future*, Advances in Global Change Research, 28, Springer, Dordrecht, pp. 79-96.
- Chandrasekhar, S. (1960). Radiative transfer, *Dover Publications Inc.*, New York, pp. 393.
- Ellison, W.; Balana, A.; Delbos, G., Lamkaouchi, K., Eymard, L., Guillou, C., & Prigent, C. (1998). New permittivity measurements of seawater, *Radio Sci.*, 33, no. 3, pp. 639-648.
- English, S. J. (1999). Estimation of temperature and humidity profile information from microwave radiances over different surface types, *J. Appl. Meteor.*, 38, pp. 1526-1541.
- Evans, F., & Stephens G. F. (1995a). Microwave radiative transfer through clouds composed of realistically shaped ice crystal. Part I: single scattering properties, *J. Atmos. Sci.*, 52, pp. 2041-2057.
- Evans, F., & Stephens G. F. (1995b). Microwave radiative transfer through clouds composed of realistically shaped ice crystal. Part II: single scattering properties, *J. Atmos. Sci.*, 52, pp. 2058-2072.
- Ferrazoli, P., Wigneron, J. P., Guerriero, L., & Chanzy, A. (2000). Multifrequency emission of wheat: Modeling and application, *IEEE Trans. Geosci. Remote Sens.*, 38, pp. 2598-2607.
- Fung, A. K. (1994). Microwave scattering and emission models and their applications, *Artech House.*, pp. 573.
- Greenwald, T. J., & Jones, A. S. (1999). Evaluation of seawater permittivity models at 150 GHz using satellite observations, *IEEE Trans. Geosci. Remote Sens.*, 37, no. 5, pp. 2159-2164.
- Grody, N. C., Weng, F., & Ferraro R. R. (2000). Application of AMSU for obtaining hydrological parameters, *In: Microwave Radiometry and Remote Sensing of the Earth's Surface and Atmosphere*, P. Pampaloni and S. Paloscia, Eds., USP Int. Science Publishers, Utrecht, pp. 339-352.
- Guillou, C., English, S. J., Prigent, C., & Jones, D. C. (1996). Passive microwave airborne measurements of the sea surface response at 89 and 157 GHz, *J. Geophys. Res.*, 101, no. C2, pp. 3775-3788.
- Hewison, T. J., & Saunders, R. W. (1996). Measurements of the AMSU-B antenna pattern. *IEEE Trans. Geosci. Remote Sensing*, 34, pp. 405-412.
- Hsu, K-L., Hong, Y., & Sorooshian, S. (2007). Rainfall estimation using a cloud patch classification map. *Measuring precipitation from space - EURAINSAT and the future*, Advances in Global Change Research, 28, Springer, Dordrecht, pp. 329-342.
- Joyce, R. J., Janowiak, J. E., Arkin, P. A., & Xie, P. (2004). CMORPH A Method that produces global precipitation estimates from passive microwave and infrared data at high spatial and temporal resolution. *J. Hydrometeor.*, 5, pp. 487-503.
- Kakar, R. K. (1983). Retrieval of clear sky moisture profiles using the 183 GHz water vapor line, *J. Climate Appl. Meteor.*, 22, pp. 1282-1289.
- Karstens, U., Simmer, C., & Ruprecht, E. (1994). Remote sensing of cloud liquid water, *Meteor. Atmos. Phys.*, 54, pp. 157-171.
- Klein, L. A., & Swift, C. T. (1977). An improved model for the dielectric constant of sea water at microwave frequencies, *IEEE Trans. Antennas Propag.*, AP25(1), pp. 104-111.

- Kummerow, C. D., Olson, W. S., & Giglio, L. (1996). A simplified scheme for obtaining precipitation and vertical hydrometer profiles from passive microwave sensors, *IEEE Trans. Geosci. Remote Sens.*, 34, pp. 1213–1232.
- Kummerow, C. D., Hong, Y., Olson, W. S., Yang, S., Adler, R. F., McCollum, J., Ferraro, R., Petty, G., Shin, D. B., & Wilheit, T. T. (2001). The evolution of the Goddard Profiling Algorithm (GPROF) for rainfall estimation from passive microwave sensors, *J. Appl. Meteor.*, 40, pp. 1801-1820.
- Levizzani, V. (2003). Clouds and rainfall by visible-infrared radiometry. *Remote Sensing of Atmosphere and Ocean from Space: Models, Instruments and Techniques*, Advances in Global Change Research, 13, Springer, pp. 127-143.
- Levizzani, V., Bauer, P., & Turk, F. J. (2007). Measuring precipitation from space - EURAINSAT and the future, *Springer*, Dordrecht, pp. 722.
- Laviola, S., & Levizzani, V. (2008). Rain retrieval using 183 GHz absorption lines. *IEEE Proc. MicroRad 2008, 10th Specialist Meeting on Microwave Radiometry and Remote Sensing of the Environment*, Firenze, 11-14 Mar., doi: 10.1109/MICRAD.2008.4579505.
- Laviola, S., & Levizzani, V. (2009a). Observing precipitation with AMSU-B opaque channels: the 183-WSL algorithm. *Proc. 4th Workshop Int. Precipitation Working Group*, Beijing, China, 13-17 October. [available at <http://www.isac.cnr.it/~ipwg/meetings/beijing/4th-IPWG-Proceedings-web-March-2009.pdf>].
- Laviola, S., & Levizzani, V. (2009b). Using water vapor lines to retrieve rainrates: the 183-WSL algorithm. *J. Appl. Meteor. Climat.*, submitted.
- Marshall, J. S., & Palmer, W. McK. (1948). The distribution of raindrops with size, *J. Meteor.*, 5, pp. 165-166.
- Rosenfeld, D. (2007). Cloud top microphysics as a tool for precipitation measurements. *Measuring precipitation from space - EURAINSAT and the future*, Advances in Global Change Research, 28, Springer, Dordrecht, pp. 61-77.
- Rosenkranz, P. W. (2001). Retrieval of temperature of moisture profiles from AMSU- and AMSU-B measurements, *IEEE Trans. Geosci. Remote Sens.*, 39, pp. 2429-2435.
- Shi, J., Chen, K. S., Li, Q., Jackson, T. J., & O'Neil, P. E. (2002). A parameterized surface reflectivity model and estimation of bare-surface soil moisture with L-band radiometer, *IEEE Trans. Geosci. Remote Sens.*, 40, pp. 2674-2686.
- Saunders, R. W., Hewison T. J., Stephen, S. J., & Atkinson, N. C. (1995). The radiometric characterization of AMSU-B, *IEEE Trans. Microwave Theory and Techniques*, 43, pp. 760-771.
- Sharkov, A. E. (2003). Passive microwave remote sensing of the Earth. Physical foundations, *Springer and Praxis Publishing Publication*, pp. 557.
- Stephen, H., & Long, D. G. (2005). Modeling microwave emissions of erg surface in the Sahara desert, *IEEE Trans. Geosci. Remote Sens.*, vol. 43, no. 12, pp. 2822-2830.
- Turk, F. J., & Mehta, A. V. (2007). Toward improvements in short-time scale satellite-derived precipitation estimates using blended satellite techniques. *Measuring precipitation from space - EURAINSAT and the future*, Advances in Global Change Research, 28, Springer, Dordrecht, pp. 281-96.
- Wang, J. R., Wilheit, T. T., & Chang, L. A. (1989). Retrieval of total precipitable water using radiometric measurements near 92 and 183 GHz, *J. Appl. Meteor.*, 28, pp. 146-154.



Advanced Microwave and Millimeter Wave Technologies Semiconductor Devices Circuits and Systems

Edited by Moumita Mukherjee

ISBN 978-953-307-031-5

Hard cover, 642 pages

Publisher InTech

Published online 01, March, 2010

Published in print edition March, 2010

This book is planned to publish with an objective to provide a state-of-the-art reference book in the areas of advanced microwave, MM-Wave and THz devices, antennas and system technologies for microwave communication engineers, Scientists and post-graduate students of electrical and electronics engineering, applied physicists. This reference book is a collection of 30 Chapters characterized in 3 parts: Advanced Microwave and MM-wave devices, integrated microwave and MM-wave circuits and Antennas and advanced microwave computer techniques, focusing on simulation, theories and applications. This book provides a comprehensive overview of the components and devices used in microwave and MM-Wave circuits, including microwave transmission lines, resonators, filters, ferrite devices, solid state devices, transistor oscillators and amplifiers, directional couplers, microstripeline components, microwave detectors, mixers, converters and harmonic generators, and microwave solid-state switches, phase shifters and attenuators. Several applications area also discusses here, like consumer, industrial, biomedical, and chemical applications of microwave technology. It also covers microwave instrumentation and measurement, thermodynamics, and applications in navigation and radio communication.

How to reference

In order to correctly reference this scholarly work, feel free to copy and paste the following:

Sante Laviola and Vincenzo Levizzani (2010). Passive Microwave Remote Sensing of Rain from Satellite Sensors, Advanced Microwave and Millimeter Wave Technologies Semiconductor Devices Circuits and Systems, Moumita Mukherjee (Ed.), ISBN: 978-953-307-031-5, InTech, Available from:
<http://www.intechopen.com/books/advanced-microwave-and-millimeter-wave-technologies-semiconductor-devices-circuits-and-systems/passive-microwave-remote-sensing-of-rain-from-satellite-sensors>

INTECH
open science | open minds

InTech Europe

University Campus STeP Ri
Slavka Krautzeka 83/A
51000 Rijeka, Croatia
Phone: +385 (51) 770 447
Fax: +385 (51) 686 166
www.intechopen.com

InTech China

Unit 405, Office Block, Hotel Equatorial Shanghai
No.65, Yan An Road (West), Shanghai, 200040, China
中国上海市延安西路65号上海国际贵都大饭店办公楼405单元
Phone: +86-21-62489820
Fax: +86-21-62489821

© 2010 The Author(s). Licensee IntechOpen. This chapter is distributed under the terms of the [Creative Commons Attribution-NonCommercial-ShareAlike-3.0 License](#), which permits use, distribution and reproduction for non-commercial purposes, provided the original is properly cited and derivative works building on this content are distributed under the same license.

IntechOpen

IntechOpen